Hydrology
2023; 11(1): 11-22
http://www.sciencepublishinggroup.com/j/hyd
doi: 10.11648/j.hyd.20231101.12
ISSN: 2330-7609 (Print); ISSN: 2330-7617 (Online)

Prerequisite Condition of Diffuse Attenuation Coefficient $K_d(490)$ for Detecting Seafloor from ICESat-2 Geolocated Photons During Shallow Water Bathymetry

Dandabathula Giribabu[1, *], Rohit Hari[1], Jayant Sharma[2], Aryan Sharma[3], Koushik Ghosh[1], Apurba Kumar Bera[1], Sushil Kumar Srivastav[4]

[1]Regional Remote Sensing Centre - West, National Remote Sensing Centre, Indian Space Research Organisation, Jodhpur, India

[2]Computer Science Department, Jaipur Engineering College and Research Centre (JECRC) University, Jaipur, India

[3]Department of Geography, Panjab University, Chandigarh, India

[4]Regional Centres, National Remote Sensing Centre, Indian Space Research Organisation, New Delhi, India

Email address:

dgb.isro@gmail.com (Dandabathula Giribabu)

[*]Corresponding author

To cite this article:

Dandabathula Giribabu, Rohit Hari, Jayant Sharma, Aryan Sharma, Koushik Ghosh, Apurba Kumar Bera, Sushil Kumar Srivastav. Prerequisite Condition of Diffuse Attenuation Coefficient $K_d(490)$ for Detecting Seafloor from ICESat-2 Geolocated Photons During Shallow Water Bathymetry. *Hydrology.* Vol. 11, No. 1, 2023, pp. 11-22. doi: 10.11648/j.hyd.20231101.12

Received: April 9, 2023; **Accepted**: April 23, 2023; **Published**: May 17, 2023

Abstract: Bathymetry refers to the depth measurement of the topographic seafloor surface and is essential geophysical data for understanding the land-ocean interplay. Recently, researchers have taken advantage of photon penetration of the green laser of NASA ICESat-2 to profile the seafloor as a part of the bathymetric mapping of shallow nearshore coastal waters. Prerequisite conditions for using the ICESat-2 geolocated photons for reconstructing the bathymetric profiles include a preference for using nighttime acquisitions followed by applying refraction correction to the water column returned photons to correct the apparent depths due to the change in the speed of light that occurs at the air-water interface. The success of detecting the seafloor from the bathymetric profiles from ICESat-2 photons will depend on the optical clarity of the water. The diffuse attenuation coefficient for downwelling irradiance, $K_d(490)$, measures how light dissipates with depth in water and indicates how strongly light intensity at 490 nm of wavelength is attenuated in the water column, providing a hint about the water clarity. In this research, we have explored ICESat-2's photon-based bathymetric mapping potential in relation to the $K_d(490)$. ICESat-2 photon data and $K_d(490)$ data from level-2 OLCI of Sentinel-3 A/B mission were acquired with overlapping dates to investigate the possible depth penetration of ICESat-2 photons in the shallow waters during clear water conditions and sediment load periods. Two nearshore study sites were chosen that are located at the head of the Bay of Bengal. This research proves that the ICESat-2 photons can successfully reflect from the seafloor in shallow waters while the optical water condition is clear, during which the $K_d(490)$ is less than 0.12 m^{-1}. On the contrary, during the periods of sediment load in the water, where the $K_d(490)$ is above 0.15 m^{-1}, the ray tracing mechanism of ICESat-2 photons has been impacted due to absorption and scattering caused by the sediments load in the water column; thus, seafloor detection by ICESat-2 photons will not be successful in sediment loaded waters. The results from this research suggest the necessity of $K_d(490)$ to be complementary data with ICESat-2 photons for successful bathymetric applications.

Keywords: Bathymetry, ICESat-2 Geolocated Photons, Diffuse Attenuation Coefficient, Sentinel-3 OLCI, $K_d(490)$

1. Introduction

The marginal marine environments, like lagoons and estuaries, lie along the boundary between the continental and coastal depositional realms and are usually dominated by tidal processes, playing a critical role in ecosystem and

engineering studies [1]. Bathymetry refers to the depth measurement of the topographic seafloor surface and is essential geophysical data in modeling and interpreting the land-ocean interplay [2]. Usually, bathymetric surveying of shallow waters by conventional ship-borne sonar techniques is slow, hazardous, and expensive [3]; due to this and the ability to capture a synoptic view, remote sensing techniques from space-borne sensors have taken the lead in generating bathymetric measurements [3-6].

Earlier, researchers have reviewed the techniques associated with satellite-derived bathymetric methods [6-10]; usually, the optical remote sensing-based methods take the cue from the principle that as depth increases, the intensity of electromagnetic energy gradually weakens due to the inherent optical properties of the water column [9], and also different wavelengths of the solar spectrum penetrate the water bodies to different depths [11]. Ashphaq et al. [7] and Duplančić et al. [10] have categorized the methods for deriving bathymetric information from optical remote sensing into empirical, semi-empirical, quasi-analytical, and analytical based on statistical, bio-optical, and physical optical properties. Similarly, Santos et al. [12] and Wiehle et al. [13] explored active remote sensing data like Synthetic Aperture Radar (SAR) to derive the bathymetric information by inferring the sea surface signatures and applying the dispersion relation on surface waters. Either the case, i.e., optical and SAR data, for final computation of bathymetric information, a priori seed point information, or in situ data is an input parameter required for estimating the depth information [11, 13]. Ashphaq et al. [7] compared various methods of deriving bathymetric information, termed non-imaging active remote sensing methods like LIDAR can provide highly accurate depth information in clear water conditions.

The National Aeronautics and Space Administration (NASA) launched Ice, Cloud and land Elevation Satellite-2 (ICESat-2) in 2018, equipped with a solo sensor, namely, Advanced Topographic Laser Altimeter System (ATLAS), a highly sensitive photon-counting system [14]. The ICESat-2 mission operates in a non-sun-synchronous orbit (thus, both the daytime and nighttime acquisitions are possible) at an average altitude of 496 km - resulting in a temporal resolution of ~91 days, during which 1387 unique ground track patterns will be covered [14]. The ATLAS sensor uses a 532 nm wavelength (green) laser, operating at a pulse repetition frequency of 10 kHz encounters a diffractive optical element to release six beams (organized as three pairs – left, near-nadir, and right), of which within each pair one beam (termed as a strong beam) has four times the energy of the other (termed as a weak beam) and has a separation of 90 m between them (illustrated in Figure 1a). The left and right paired beams are both 3.3 km apart from the nadir most paired beam, and each beam will have a nominal 17 m diameter footprint with an along-track sampling interval of 0.7 m [14]. Once these laser beams hit the earth's surface, reflected photons are recorded by the photon-counting telescope mounted on the ATLAS sensor to yield the range measurements. Data related to the ICESat-2 platform (like position, orientation, attitude, orbital velocity), laser pointing vectors, pulse emission timing, and the range measurements will be assimilated to generate the latitude, longitude, and ellipsoidal heights for each geolocated photon [14, 15].

At ground stations, science teams of ICESat-2 will process and distribute various levels of data products through a web portal maintained by National Snow and Ice Data Centre (NSIDC) [16]. Global geolocated photon data available as Level-2A product under the nomenclature ATL03 contains height above the WGS84 ellipsoid (ITRF2014 reference frame), latitude, longitude, and time for all photons downlinked by the ATLAS instrument on board the ICESat-2 [17]. Even though ATL03 is a non-imaging product, attributes like latitude and longitude enable the geospatial community to infer the data in the spatial domain. An along-track sequence of geolocated photons from the ATL03 data product allows one to generate profiles to essay the earth's surface variation (the concept shown in Figure 1 for a subset of photon data over Shaheed Dweep / Niel Islands of Andaman and Nicobar, India).

The primary mission objectives of the ICESat-2 profiling system aimed at cryosphere studies [14], but the geolocated photons accumulated from this mission have proven to be resourceful data that can foster the research areas like climate change and global warming, meteorology, natural sciences, land and topography, hydrology and bathymetry [18-20]. Regarding the accuracy of the geolocated photons, performance assessment done by various researchers confirms meeting the sensor's specification [18, 19].

Towards extending the applications beyond the cryosphere, Neuenschwander and Magruder [21] first explored the utility of distinguishing terrain and canopy from the profiles generated from the ICESat-2 geolocated photons; the concept is illustrated in Figure 1c for an island. There need no required pre-processing methods for terrain and canopy applications of ICESat-2 photons. However, for hydrological applications of ICESat-2 photons, specifically, there needs to be a preference for nighttime acquisitions; this is because the background noise caused by solar spectral radiation significantly impacts the detection performance of lidar [22, 23].

Parrish et al. [24] are credited for evaluating the performance of ICESat-2 photons towards bathymetric studies, which highlighted the need to apply refraction correction to the depths because of the change in speed of light that occurs at the air-water interface, else, horizontal and vertical errors in the estimation will prevail, this is because the refractive index of air and water are different. However, the maximum horizontal offset due to the refraction tends to be 9 cm at a water depth of 30 m and can negotiate due to the beam footprint of 17 m [24]. Studies done by Parrish et al. [24] confirm that using ICESat-2 photons, seafloor detection in water depths of up to ~40 m is possible. However, the maximum depth a photon can reflect depends on the water's transparency. Further, Ma et

al. [25] suggested applying corrections to eliminate sea level variabilities induced by waves and tides. During the final computation of depth, one needs to convert the ellipsoidal heights of ICESat-2 photons to orthometric heights [26-28].

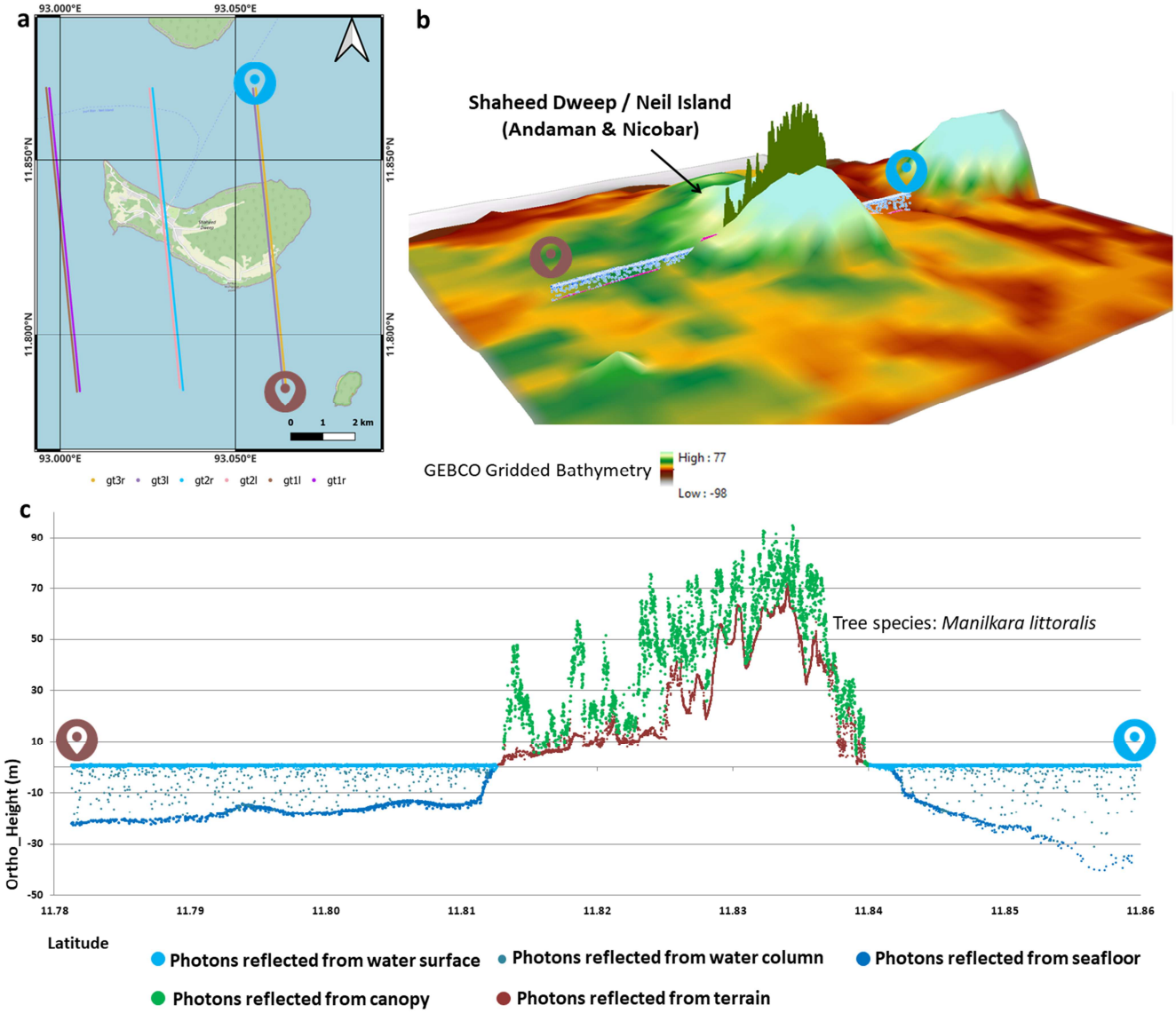

Figure 1. *Concept of profiling from ICESat-2 geolocated photons. (a) Subsets of three pairs of beams from ICESat-2 ATLAS sensor acquired on 2019-Dec-26 over Shaheed Dweep/Niel island (Andaman & Nicobar, India). (b) 3D representation of profiling using ICESat-2 geolocated photons for one of the beams (gt1l strong) on the height map generated from GEBCO gridded bathymetry data over Shaheed Dweep/Niel Island. (c) 2D profile showing orthoheight on y-axis and latitude on x-axis over the Sheed Dweep/Niel Island, clearly showing the photons reflected from the water surface, water column, and seafloor. Over the land, photons reflected from the canopy and terrain can be visualized.*

By latest, various studies validating the performance of ICESat-2 photons for deriving water depths reported root mean square error (RMSE) ranging between 0.20 to 0.89 m [26, 29, 30], which is, by far, significantly high accurate measurements from the current operational space-borne active sensor systems.

This research is oriented towards finding the optimal clear water conditions for successful seafloor detection by ICESat-2 photons; thereby, the results should enable the bathymetric investigators to select the data acquired during the optically clear water conditions. The diffuse attenuation coefficient for downwelling irradiance, $K_d(\lambda)$ (in m^{-1}), where λ is the wavelength of light, is a measure of how light dissipates with depth in water; it indicates how strongly light intensity at a specified wavelength is attenuated within the water column. The presence of scattering particles in the water column, either organic or inorganic materials, will influence the process of light transportation. Hence K_d acts as a measurement of water clarity [31, 32]. Usually, K_d is computationally feasible using remote sensing techniques [33] and is of interest to the scientific fraternity requiring a prediction of light propagation qualities of seawater, especially for active/passive optical systems for mapping the bathymetry [31, 33]. The current operational empirical

algorithms to compute diffuse attenuation coefficient at λ = 490 nm, termed as $K_d(490)$, is estimated using the ratio of water-leaving radiances at blue and green wavelengths, discussed by Austin et al. and Lee et al. [31, 33] and indicates the turbidity presence in the water column; thus, acts as an indicator for how visible light in the blue to green region of the spectrum penetrates within the water column. In general, the pixel values of K_d data generated from the remote sensing methods vary from 0 to 10 m^{-1}, where values toward zero indicate less light attenuation and, thus, transparent or clear water conditions. Conversely, larger K_d values indicate greater opaque like in sediment-dominant waters.

Ocean and Land Colour Instrument (OLCI) is one of the instruments of the Sentinel-3 mission, which is aimed at measuring sea surface topography, sea and land surface temperature, and ocean and land surface color with high accuracy and reliability to support ocean forecasting systems, environmental monitoring, and climate monitoring [36]. Sentinel-3 OLCI level-2 series of data product services comprises $K_d(490)$ as a raster band helpful to characterize the transparency from the spectrum of the normalized water-leaving reflectances based on the bands with central λ = 490 nm and λ = 560 nm [37, 38] that was developed using the method proposed by Morel et al. [35]. Earlier, validation of Sentinel-3 OLCI water quality products with field-level data done by Kyryliuk et al. [39] and Glukhovets et al. [40] resulted in confirming the reliable accuracies due to relatively low bias. OLCI data products from Sentinel-3 A/B platforms are available for global coverage with a spatial resolution of 300 m and almost daily temporal resolution [37].

In this research, two study sites falling in the coastal waters of the Bay of Bengal were selected to inspect the relationship between refraction-corrected seafloor returned ICESat-2 photons and seawater quality inferred from the $K_d(490)$ from the Sentinel-3 OLCI. Analysis was done on the data acquired during clear water and turbid-prone seasons to instigate the behavior of ICESat-2 photons in the water column. Even though the ATLAS sensor uses a 532 nm wavelength (green) laser, the open-accessible $K_d(490)$ data is available daily; this enables one to use and crosscheck the water quality before estimating the depth from ICESat-2 geolocated photons.

2. Material and Methods

2.1. Study Area

The two test sites selected for this research are located in the eastern coastal area of the Indian subcontinent (Figures 2b and 2c show the extent of these test sites). The first test site is located on the eastern side of Kavali town, and the second is located on the eastern side of Nellore city. The east coast of India termed the head of the Bay of Bengal, is 120 km wide, characterized by well-defined beaches, sand dunes and spits, many lagoonal lakes associated with backwater swamps, and estuaries [41]. Most of the Indian east coast is relatively calm from January to March; however, other seasons are influenced by dynamic factors arising from incessant rainfall and tropical cyclones originating from the monsoon transition and monsoon periods [42-44]. From June to September, the east coast waters intake heavy sedimentation from peninsular river discharge [45]. The rationale for selecting these test sites is that the depth to the seafloor adjoining the coast is less than 40 m [46]; thus, during the clear water condition, there is a possibility for ICESat-2 photons to penetrate up to the seafloor as per Parrish et al. [24]. Similarly, both the test sites exhibit clear water conditions (during January-March) and sediment accumulation post-June month. Hence these two conditions are conducive to observing the behavior of ICESat-2 photons in the water column in relation to $K_d(490)$.

2.2. Datasets

Table 1 shows the details of the datasets used in this investigation. Primarily, the datasets include ATL03, a level-2A ICESat-2 photon data product, $K_d(490)$ product from Level-2 OLCI product of Sentinel-3 A/B, and seafloor information derived from the General Bathymetric Chart of the Ocean (GEBCO) gridded bathymetry data.

For both the test sites in this research, subsets of ICESat-2 ATL03 data for a ~50 km length were downloaded from the NSIDC web portal available at https://nsidc.org/data/icesat-2 [16] in Hierarchical Data Format (HDF). Data pertaining to two periods, one during the clear water season (January to March) and the other during the sediment accumulation period (during and after June), were opted for this investigation. The separation between these two beams is ~500 m, and as a precursor condition, ICESat-2 beams for both seasons were considered nighttime acquisitions.

Correspondingly, for the same dates as acquired by the ICESat-2, within +/- 24 hours, Level-2 OLCI data products from the Sentinel-3 A/B mission were downloaded from the web portal titled Copernicus Data Space Ecosystem, which is an open ecosystem that provides free instant access to a wide range of data and services from the Copernicus Sentinel missions [47]. However, for test site 2, during the non-clear water season, a composite product of $K_d(490)$ was generated used from the data obtained from two dates, as mentioned in Table 1; this is to compensate for the missing pixel values (due to cloud) in a single date imagery.

GEBCO_2002 grid is a global gridded terrain model that provides elevation/depth information for land and oceans, respectively, and is available at a 15 arc-second (450 m) from the web portal at https://www.gebco.net/ [46]. In this investigation, we used the seafloor information from GEBCO to compare the maximum depth detected by ICESat-2 photons for both study areas.

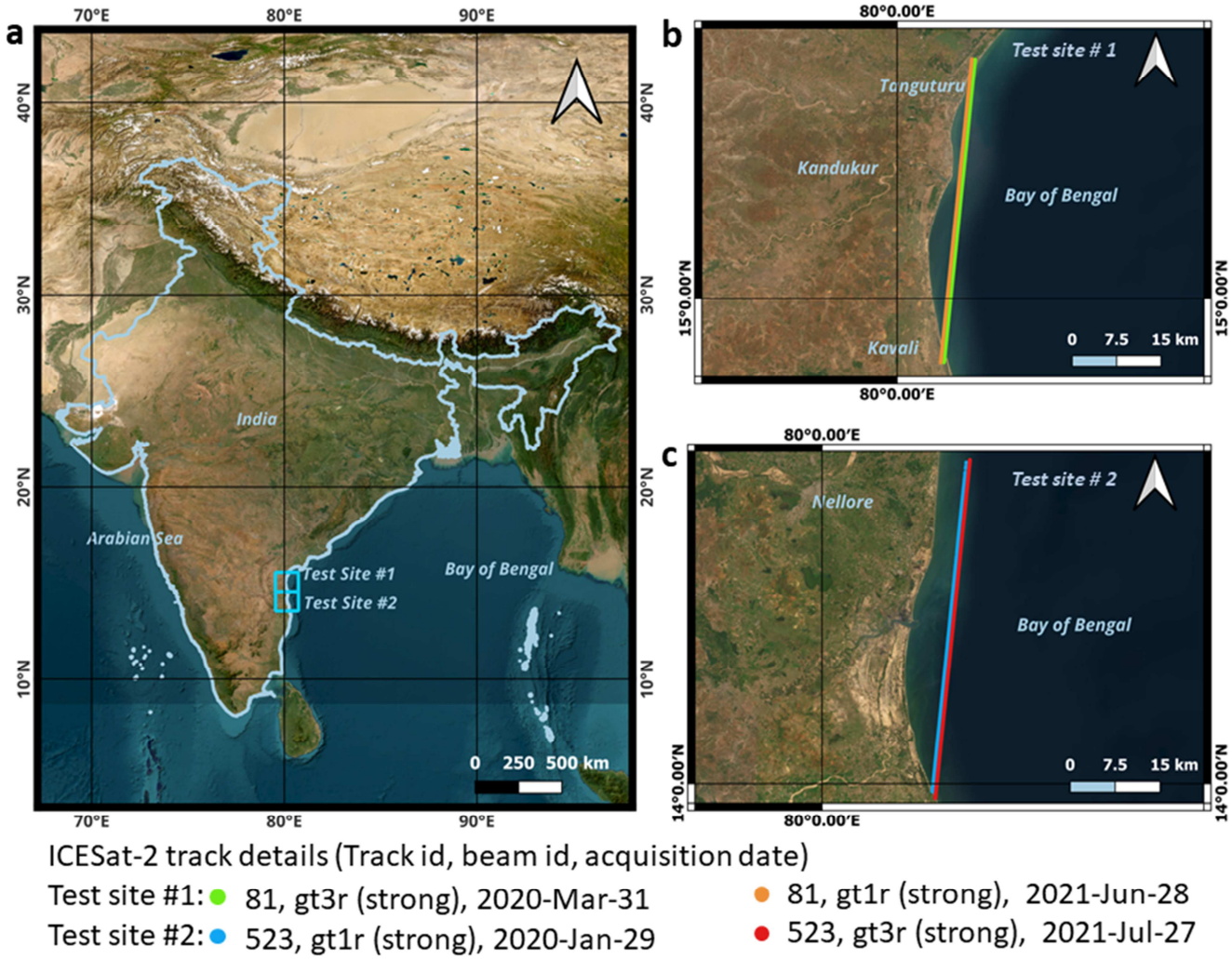

Figure 2. *Location map of the study area. (a) Location of the two test sites. (b) Coastal waters spread at the eastern Kavali town used as test site #1 with an overlay of beams from ICESat-2 (c) Coastal waters spread over the eastern Nellore city used as test site #2 with an overlay of beams from ICESat-2.*

Table 1. *Details of datasets used to infer the behavior of ICESat-2 photons in the water column in relation to $K_d(490)$. $K_d(490)$ has been derived from Level-2A OLCI imagery of Sentinel-3 A/B mission.*

Test site details	ICESat-2 ATL03 product (Track id, beam id & acquisition date/local time)	Sentinel-3 A/B OLCI Level-2A data product (Platform & acquisition date)
Test site #1: Coastal waters at the eastern Kavali town, Andhra Pradesh, India	81, gt3r (strong) & 2020-Mar-31/02:10 Hrs. 81, gt1r (strong) & 2021-Jun-28/05:00 Hrs.	S3B & 2020-Mar-30 S3A & 2021-Jun-29
Test site #2: Coastal waters at the eastern Nellore town, Andhra Pradesh, India	523, gt1r (strong) & 2020-Jan-29/05:00 Hrs. 523, gt3r (strong) & 2021-Jul-27/03:40 Hrs.	S3A & 2020-Jan-29 S3A & 2021-Jul-27 & S3B & 2021-Jul-28

2.3. Methodology

Figure 3 shows the methodology implemented in this investigation. The location information (latitude and longitude) and ellipsoidal height of every successful photon event were retrieved from the ICESat-2 ATL03 data product. The ATL03 dataset provides a confidence attribute ranging from 0 (noisy) to 4 (being high-quality signal), enabling the distinction of qualified signal photons from noise photons. For water-related studies, one needs to consider all the photons irrespective of the confidence value, especially for the successful detection of seafloor [25]. Default heights in the ATL03 data product were converted to orthometric heights using the geodetic utilities provided at https://www.unavco.org [49]. ICESat-2 ATL03 data after undergoing numerous corrections to remove the errors accumulated due to solid earth deformation, ocean tides, and atmospheric delay, needs refraction correction; in this research, the method suggested by Parrish et al. [24] and endorsed by Ma et al. and Ranndal et al. [25, 50] was implemented. This step eliminated the vertical errors accrued due to the difference in the air and water refractive index, providing the absolute depth.

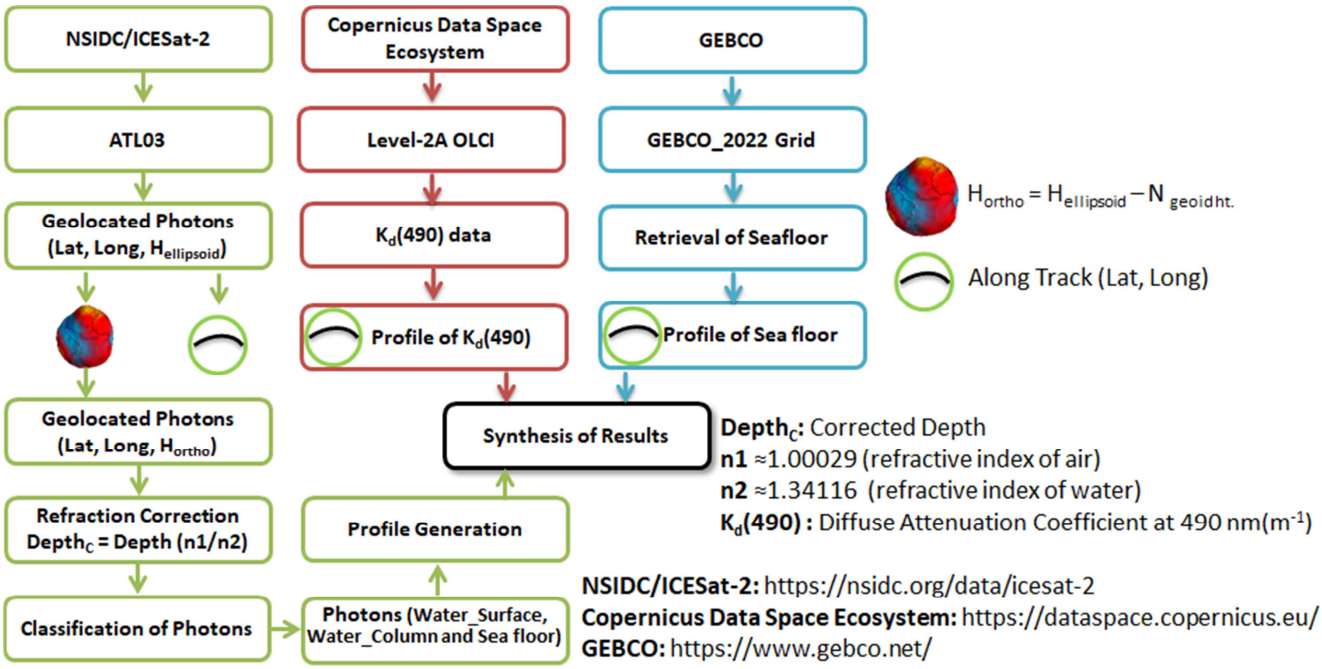

Figure 3. *Flowchart of the methodology used to infer the behavior of ICESat-2 photons in the shallow waters in relation to $K_d(490)$.*

Once refraction correction is done, latitude, longitude, and corrected depth were fed to the Density-Based Spatial Clustering of Applications with Noise (DBSCAN) algorithm to classify the photons reflected from the water surface, water-column, and seafloor. All these classes of photons were used to generate bathymetric profiles. Generally, the bathymetric profiles generated from the ICESat-2 geolocated photons consist of orthometric heights (depth in m) on the y-axis and the x-axis on the latitude along the ground track.

Sentinel Application Platform (SNAP) is a free and open-source toolbox for scientifically exploiting the data from Sentinel missions [48]. SNAP software was used to perform the standard pre-processing steps and to subset the $K_d(490)$ layer from the Level-2 OLCI product of the Sentinel-3 A/B mission. Profiles from the $K_d(490)$ pixels and GEBCO_2022 grid were generated along the track of ICESat-2 geolocated photons. Bathymetric profiles generated from the ICESat-2 geolocated photons and the $K_d(490)$ datasets were used to infer the maximum depth detectability of ICESat-2 photons during clear and non-clear water conditions. Profile from the GEBCO bathymetric data is used to compare the seafloor with that of ICESat-2 detected seafloor.

3. Results

Figures 4 and 5 show the results for test sites #1 and #2, respectively. In particular, Figures 4a and 5a show the bathymetric profiles generated from the ICESat-2 geolocated photons after refraction correction during clear water conditions for respective study sites. Similarly, Figures 4c and 5c show the bathymetric profiles for individual study sites during the sediment accumulation period. In these profiles, the y-axis has depth (in meters), and the x-axis shows the along-track latitude.

In the same lines, Figure 4b and 5b shows the profile generated from the $K_d(490)$ layer obtained from the level-2 OLCI imagery of Sentinel-3 A/B during clear water conditions. In contrast, Figure 4d and 5d shows the profile generated from $K_d(490)$ layer during the sediment accumulation period; for these profiles, the y-axis consist of $K_d(490)$ (in m^{-1}), and the x-axis has the along-track latitude similar to that of corresponding bathymetric profiles generated from ICESat-2 geolocated photons.

In the bathymetric profiles, photons reflected from the water surface, water column, and the seafloor are distinguished with different color schemes; to bind and compare with a modeled assisted seafloor with that of the ICESat-2 detected seafloor, surface profile from the GEBCO gridded bathymetric data has been overlaid.

For test site #1, i.e. coastal waters at the east of Kavali town, during the clear water season, sea floor up to a depth of ~16 m is evident from the bathymetric profile (Figure 4a), which is also quite close intersect to the seafloor derived from the GEBCO gridded bathymetry. During this, it is observed that the $K_d(490)$ derived from the level-2 OLCI of Sentinel-3 A/B is always less than 0.12 m^{-1} (Figure 4b). Whereas, during the sediment accumulation period, photons penetrated only upto ~8 m into the water column (Figure 4c) yet the maximum seafloor is at a depth of ~16 m. Corresponding to this period, the $K_d(490)$ is ranging between 0.15 to 0.4 m^{-1} which is depicted in Figure 4d.

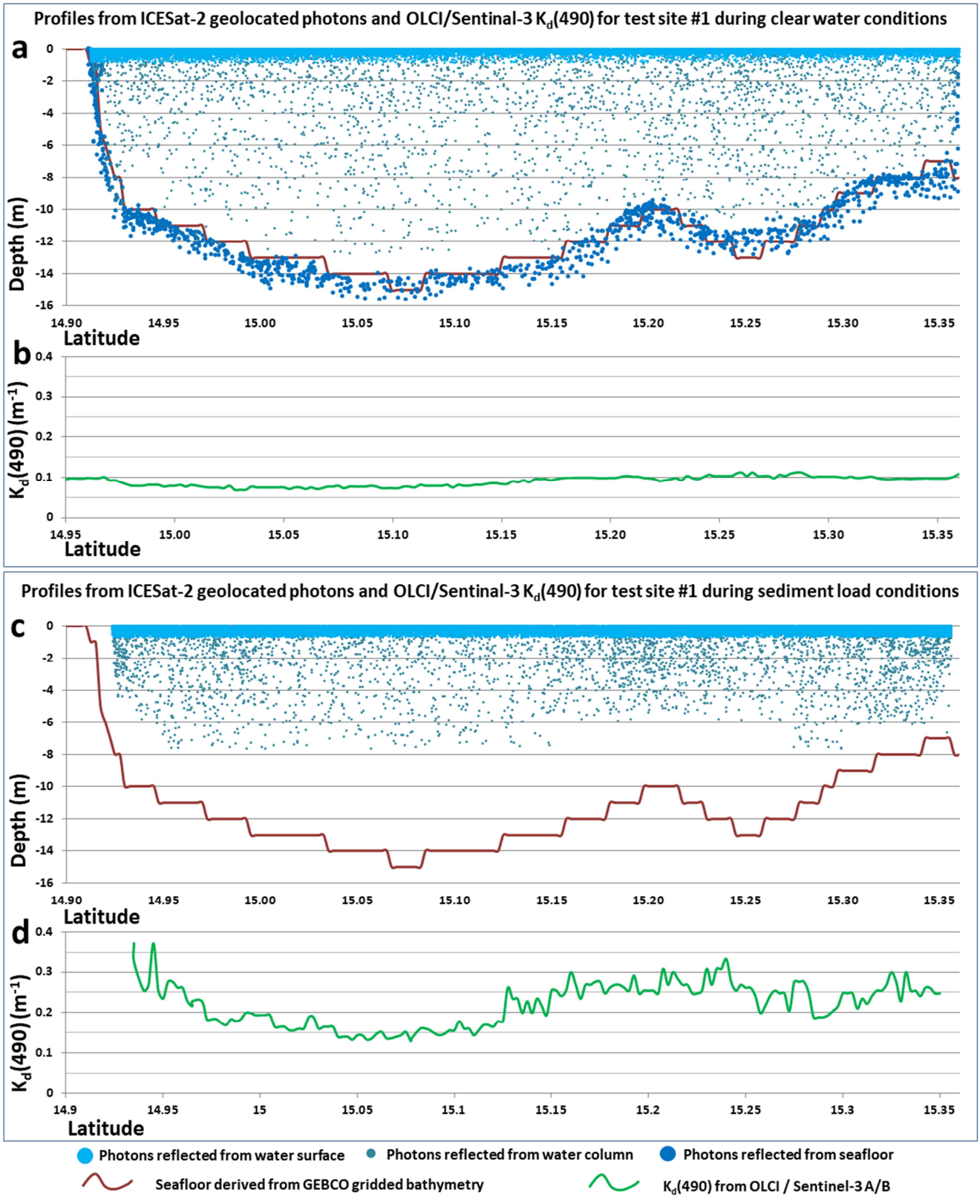

Figure 4. *Bathymetric profile from ICESat-2 geolocated photons and corresponding profile of K_d(490) derived from level-2 OLCI of Sentinel-3 A/B mission for the extent containing shallow coastal waters at the eastern part of Kavali town, Andhra Pradesh, India. The ICESat-2 and Sentinel-3 acquisition overlap is +/- 24 hours. (a) Bathymetric profile during clear water conditions with an overlay of the surface profile from GEBCO gridded bathymetric data. (b) Profile generated from the K_d(490) layer for the same extent as shown in (a). (c) Bathymetric profile during sediment accumulation period with an overlay of the surface profile from GEBCO gridded bathymetric data. (d) Profile generated from the K_d(490) layer for the same extent as shown in (c).*

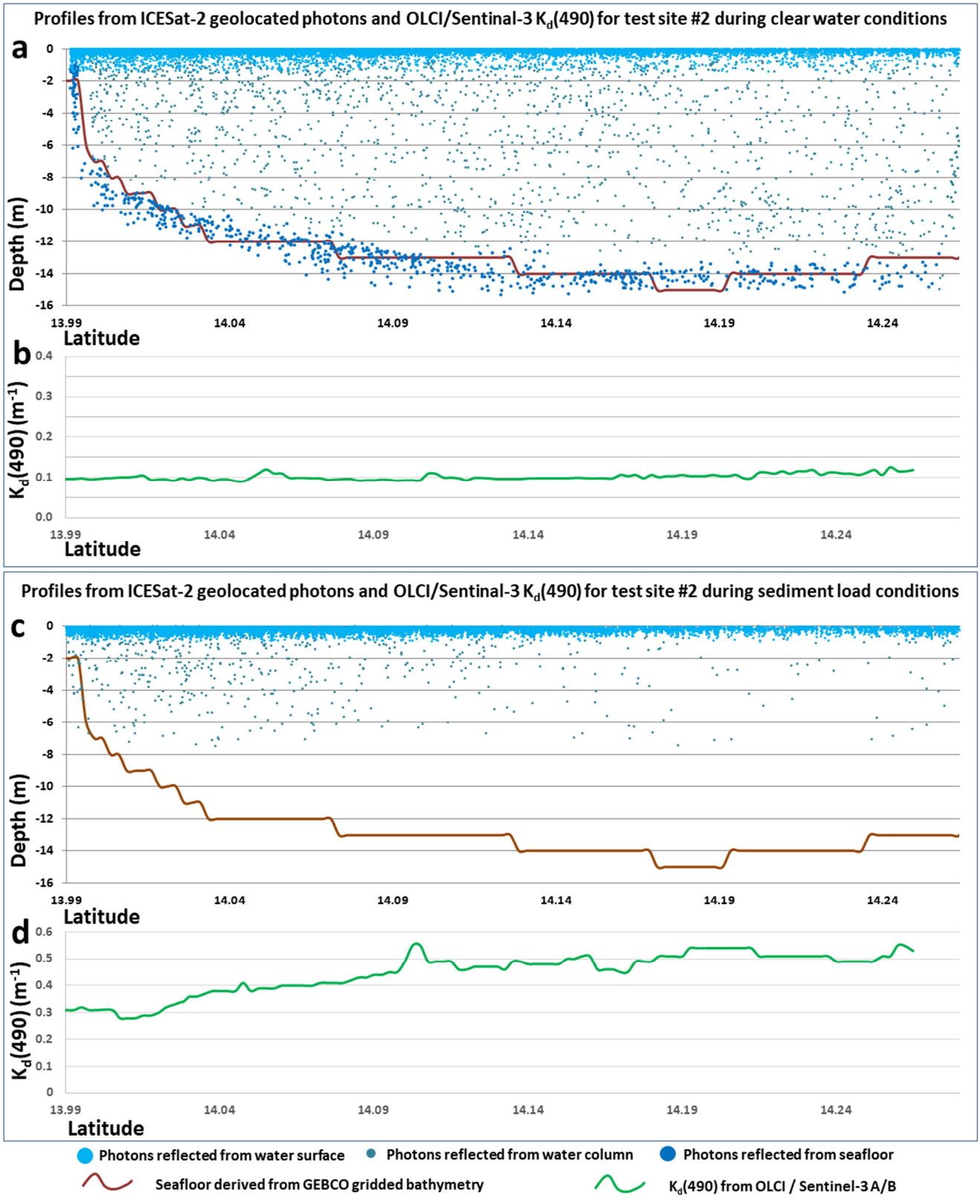

Figure 5. *Bathymetric profile from ICESat-2 geolocated photons and corresponding profile of $K_d(490)$ derived from level-2 OLCI of Sentinel-3 A/B mission for the extent containing shallow coastal waters at the eastern part of Nellore city, Andhra Pradesh, India. The ICESat-2 and Sentinel-3 acquisition overlap is +/- 24 hours. (a) Bathymetric profile during clear water conditions with an overlay of the surface profile from GEBCO gridded bathymetric data. (b) Profile generated from the $K_d(490)$ layer for the same extent as shown in (a). (c) Bathymetric profile during sediment accumulation period with an overlay of the surface profile from GEBCO gridded bathymetric data. (d) Profile generated from the $K_d(490)$ layer for the same extent as shown in (c).*

For test site #2, i.e., coastal waters at the east of Nellore city, during the clear water season, the seafloor up to a depth of ~15 m is evident from the bathymetric profile (Figure 5a), which is also quite close intersect to the seafloor derived from the GEBCO gridded bathymetry. During this, it is observed that the $K_d(490)$ derived from the level-2 OLCI of Sentinel-3 A/B is always less than 0.12 m^{-1} (Figure 5b). Whereas, during the sediment accumulation period, photons penetrated only up to ~6 m into the water column (Figure 5c), the maximum seafloor is at a depth of ~16 m. Corresponding to this period, the $K_d(490)$ ranges between 0.3 to 0.5 m^{-1}, depicted in Figure 5d.

4. Discussion

Coastal shallow waters are dynamic due to the intersection of land, ocean, and atmosphere, thus exhibiting significant variability in physical and biogeochemical cycles due to the intake of massive terrestrial material inputs [51]. This terrestrial material, in the form of silt, clay, inorganic, and organic matter such as algae, plankton, and decaying material, either dissolved or particulate/suspended, is the main flux of material from the continents to the coastal waters that will influence the optical attributes of the shallow waters. Turbidity is an optical determination of the water clarity [52] and affects the physical look of the water. Water clarity is a physical characteristic defined by how transparent the water is and determined by the depth that light penetrates in water. The more sediments in the water, the more the light attenuates, i.e., diminished by scattering (changing the direction of propagation) or absorption before reaching the seabed [53, 54]. The diffuse attenuation coefficient $K_d(\lambda)$ is considered an index of visual water clarity for shallow waters that can be detected using remote sensing methods [55-57].

The maximum depth of these shallow water at test sites #1 and #2 indicated by the GEBCO gridded bathymetric data is ~16 m and ~15 m, respectively. P rofiles generated using the ICESat-2 geolocated photons follow a similar seafloor trend as obtained by GEBCO gridded bathymetry (refer to Figures 4a and 5a during clear water conditions for both the test sites. Earlier researchers confirm similar results in various study areas while validating the potential of nearshore bathymetry of ICESat-2 photons [24, 29, 50, 58-60]; however, our research has parallelly retrieved the $K_d(490)$ from level-2 OLCI of Sentinel-3 A/B mission overlapping with the same acquisition with that of ICESat-2, indicated a value less than 0.12 m^{-1} (refer to Figure 4b and 5b).

During the sediment accumulation periods, for both the test sites, the seafloor is not seen in the bathymetric profile created using the ICESat-2 photons (refer to Figure 4c and 5c); however, few photons have reflected from the water column up to the certain extent of depth which is lesser than the depth of the seafloor (as indicated by the surface profile of GEBCO gridded bathymetric data). During this period, $K_d(490)$ values range between 0.15 to ~0.4 m^{-1} and 0.3 to 0.5 m^{-1} for test sites #1 and #2, respectively (refer to Figure 4c and 5c). Especially for test site #2, where the $K_d(490)$ is greater than 0.3 m^{-1}, the density of ICESat-2 photons penetrating the water column is very low. Earlier researchers recorded similar observations that in the turbid dominant water, the ICESat-2 photons may not be able to penetrate till the seabed but attenuate in between anywhere in the water column [61-64]. The primary reason for this attenuation is that the photons' ray tracing mechanism is affected by absorption and scattering in the overlying water column [11, 53].

Parrish et al. [24], while analyzing the bathymetric mapping performance through ICESat-2 photons at four study sites, used $K_d(490)$ derived from Visible Infrared Imaging Radiometer Suite (VIIRS), where the acquisition dates of $K_d(490)$ and ICESat-2 of same dates; the observation from their research is that the maximum depth penetration up to the seafloor is successful when $K_d(490)$ is less than 0.12 m^{-1}. The results from our study confirm the observations made by Parrish et al. [24].

5. Conclusion

Bathymetry refers to the depth measurement of the topographic seafloor surface and is essential geophysical data for understanding the land-ocean interplay. Nearshore bathymetry or mapping the seafloor at shallow coastal waters is challenging because instruments such as global navigation satellite system (GNSS) receivers, surveying instruments, and total stations need to be optimized to operate in the water. Acoustics sensors are usually mounted on ships for bathymetric mapping, but ship sailing faces dangers in the shallow waters of nearshores. Remote sensing-based bathymetric methods are mostly empirical and need seed points as input. Active remote sensing methods like lidar can provide highly accurate depth information in clear water conditions. This research explored NASA ICESat-2's photon-based bathymetric mapping potential in relation to the Kd(490).

ICESat-2 photons and $K_d(490)$ data from level-2 OLCI of Sentinel-3 A/B mission were acquired with overlapping dates to investigate the possible depth penetration of ICESat-2 photon in the shallow waters during clear water conditions and sediment load period. Two study sites were chosen for this research and are located at the head of the Bay of Bengal. This research proves that the ICESat-2 photons successfully reflected from the seafloor in the coastal waters while the optical water condition is clear, during which the $K_d(490)$ is always less than 0.12 m^{-1}. On the contrary, during the periods of sediment load in the coastal waters and $K_d(490)$ is above 0.15 m^{-1}, the ray tracing mechanism of ICESat-2 photons was impacted due to absorption and scattering because of the sediments present in the water column; thus, seafloor detection by ICESat-2 photons was not successful. Moreover, in one of the test sites, while the $K_d(490)$ is 0.3 to 0.5 m^{-1}, photons have yet to reach the depth of the water column.

Earlier researchers have recorded certain prerequisite conditions when using ICESat-2 photons for creating bathymetric profiles; these include using nighttime acquisitions and applying refraction corrections to the depth measurements. Our research suggests the necessity of diffuse

attenuation coefficient $K_d(490)$ to be lesser than 0.12 m^{-1}, during which successful seafloor can be detected in the bathymetric profiles generated by the ICESat-2 geolocated photons in shallow waters. $K_d(490)$, part of level-2 OLCI from Sentinel-3 A/B mission, which is available for a global extent and has the daily temporal resolution, can be the best complementary data with ICESat-2 photons for successful bathymetric applications.

Acknowledgements

The authors gratefully acknowledge the science team of ICESat-2 for providing access to the data. Similarly, the authors sincerely thank the science teams of Sentinel-3 A/B mission and GEBCO for providing access to their original data sources. This work was conducted with the infrastructure provided by National Remote Sensing Centre (NRSC), for which the authors were indebted to the Director, NRSC, Hyderabad. We acknowledge the continued support and scientific insights from Dr. Rakesh Paliwal, Mr. Rakesh Fararoda, Mr. Manish K Verma, and other staff members of Regional Remote Sensing Centre - West, NRSC/ISRO, Jodhpur.

References

[1] Boggs, S. A. Jr. (2012). *Principles of stratigraphy and sedimentology* (5th edition). Prentice Hall, Upper Saddle River, NJ.

[2] Vogt, P. R., & Tucholke, B. E. (1986). *Imaging of the ocean floor*. In: Vogt, P. R., & Tucholke, B. E. (Eds.). *The western north Atlantic region,* Geological Society of America, Boulder. pp. 19-44.

[3] Lyzenga, D. R. (1985). Shallow-water bathymetry using combined lidar and passive multispectral scanner data. *Int. J. Remote Sens.*, 6 (1), 115-125. doi: 10.1080/01431168508948428.

[4] Vyas, N. K, & Andharia, H. I. (1988). Coastal bathymetric studies from space imagery. *Mar. Geod.*, 12 (3), 177-187.

[5] Abdallah, H., Bailly, J. S., Baghdadi, N. N., Saint-Geours, N., & Fabre, F. (2012). Potential of space-borne LiDAR sensors for global bathymetry in coastal and inland waters. *IEEE J. Sel. Top. Appl. Earth. Obs. Remote Sens.*, 6 (1), 202-216. doi: 10.1109/JSTARS.2012.2209864.

[6] Salameh, E., Frappart, F., Almar, R., Baptista, P., Heygster, G., Lubac, B.,... & Laignel, B. (2019). Monitoring beach topography and nearshore bathymetry using spaceborne remote sensing: A review. *Remote Sens.*, 11 (19), 2212. doi: 10.3390/rs11192212.

[7] Ashphaq, M., Srivastava, P. K., & Mitra, D. (2021). Review of near-shore satellite derived bathymetry: Classification and account of five decades of coastal bathymetry research. *J. Ocean Eng. Sci.*, 6 (4), 340-59. doi: 10.1016/j.joes.2021.02.006.

[8] Cesbron, G., Melet, A., Almar, R., Lifermann, A., Tullot, D., & Crosnier, L. (2021). Pan-European Satellite-Derived Coastal Bathymetry—Review, User Needs and Future Services. *Front. Mar. Sci.*, 8, 740830. doi: 10.3389/fmars.2021.740830.

[9] Evagorou, E., Argyriou, A., Papadopoulos, N., Mettas, C., Alexandrakis, G., & Hadjimitsis, D. (2022). Evaluation of Satellite-Derived Bathymetry from High and Medium-Resolution Sensors Using Empirical Methods. *Remote Sens.*, 14 (3), 772. doi: 10.3390/rs14030772.

[10] Duplančić Leder, T., Baučić, M., Leder, N., & Gilić, F. (2023). Optical Satellite-Derived Bathymetry: An Overview and WoS and Scopus Bibliometric Analysis. *Remote Sens.*, 15 (5), 1294. doi: 10.3390/rs15051294.

[11] Lu, X., Hu, Y., Omar, A., Yang, Y., Vaughan, M., Rodier, S., Garnier, A., Ryan, R., Getzewich, B., & Trepte, C. (2022). Nearshore bathymetry and seafloor property studies from Space lidars: CALIPSO and ICESat-2. *Opt. Express*, 30 (20): 36509-36525. doi: 10.1364/OE.471444.

[12] Santos, D., Fernández-Fernández, S., Abreu, T., Silva, P. A., & Baptista, P. (2022). Retrieval of nearshore bathymetry from Sentinel-1 SAR data in high energetic wave coasts: The Portuguese case study. *Remote Sen. Appl.: Soc. Environ.*, 25, 100674. doi: 10.1016/j.rsase.2021.100674.

[13] Wiehle, S., Pleskachevsky, A., & Gebhardt, C. (2019). Automatic bathymetry retrieval from SAR images. *CEAS Space J.*, 11 (1), 105-14. doi: 10.1007/s12567-018-0234-4.

[14] Markus, T., Neumann, T., Martino, A., Abdalati, W., Brunt, K., Csatho, B., Farrell, S., Fricker, H., Gardner, A., Harding, D., & Jasinski M. (2017). The Ice, Cloud, and land Elevation Satellite-2 (ICESat-2): science requirements, concept, and implementation. *Remote Sens. Environ.*, 190, 260-73. doi: 10.1016/j.rse.2016.12.029.

[15] Neumann, T. A., Martino, A. J., Markus, T., Bae, S., Bock, M. R., Brenner, A. C., Brunt, K. M., Cavanaugh, J., Fernandes, S. T., Hancock, D. W., & Harbeck K. (2019). The Ice, Cloud, and Land Elevation Satellite–2 Mission: A global geolocated photon product derived from the advanced topographic laser altimeter system. *Remote Sens. Environ.*, 233, 111325. doi: 10.1016/j.rse.2019.111325.

[16] NSIDC, (National Snow and Ice Data Center). (2023). https://nsidc.org/data/icesat-2.

[17] Neumann, T. A., Brenner, A., Hancock, D., Robbins, J., Saba, J., Harbeck, K., Gibbons, A., Lee, J., Luthcke, S. B., & Rebold, T. (2021). ATLAS/ICESat-2 L2A global geolocated photon data, version 5. Boulder, Colorado USA. NASA National Snow and Ice Data Center Distributed Active Archive Center. doi: 10.5067/ATLAS/ATL03.005.

[18] Magruder, L., Neumann, T., & Kurtz, N. (2021). ICESat-2 Early Mission Synopsis and Observatory Performance. *Earth Space Sci.*, 8 (5), e2020EA001555. doi: 10.1029/2020EA001555.

[19] Martino, A. J., Neumann, T. A., Kurtz, N. T, & McLennan, D. (2019). ICESat-2 mission overview and early performance. In: Proceedings of SPIE 11151, Sensors, Systems, and Next-Generation Satellites - XXIII, 111510C, Bellingham. doi: 10.1117/12.2534938.

[20] Brown, M. E., Arias, S. D., & Chesnes, M. (2022). Review of ICESat and ICESat-2 literature to enhance applications discovery. *Remote Sens. Appl.: Soc. Environ.*, 100874. doi: 10.1016/j.rsase.2022.100874.

[21] Neuenschwander, A. L., & Magruder, L. A. (2019). Canopy and terrain height retrievals with ICESat-2: A first look. *Remote Sens.*, 11 (14), 1721. doi: 10.3390/rs11141721.

[22] Jasinski, M. F., Stoll, J. D., Cook, W. B., Ondrusek, M., Stengel, E., & Brunt, K. (2016). Inland and near-shore water profiles derived from the high-altitude Multiple Altimeter Beam Experimental Lidar (MABEL). *J. Coast Res.*, 76 (sp1), 44-55. doi: 10.2112/si76-005.

[23] Dandabathula, G., Bera, A. K., Sitiraju, S. R., & Jha, C. S. (2021). Inferring Lake Ice Status Using ICESat-2 Photon Data. *Remote Sens. Earth Syst. Sci.*, 4 (4), 264-79. doi: 10.1007/s41976-022-00067-4.

[24] Parrish, C. E., Magruder, L. A., Neuenschwander, A. L., Forfinski-Sarkozi, N., Alonzo, M., & Jasinski, M. (2019). Validation of ICESat-2 ATLAS bathymetry and analysis of ATLAS's bathymetric mapping performance. *Remote Sens.*, 11 (14), 1634. doi: 10.3390/rs11141634.

[25] Ma, Y., Xu, N., Liu, Z., Yang, B., Yang, F., Wang, X. H., & Li, S. (2020). Satellite-derived bathymetry using the ICESat-2 lidar and Sentinel-2 imagery datasets. *Remote Sens. Environ.*, 250, 112047. doi: 10.1016/j.rse.2020.112047.

[26] Parrish, C. E., Magruder, L., Herzfeld, U., Thomas, N., Markel, J., Jasinski, M., Imahori, G., Herrmann, J., Trantow, T., Borsa, A., & Stumpf, R. (2022). ICESat-2 Bathymetry: Advances in Methods and Science. In: OCEANS 2022, Hampton Roads: IEEE, 1-6. doi: 10.1109/OCEANS47191.2022.9977206.

[27] Yang, J., Ma, Y., Zheng, H., Xu, N., Zhu, K., Wang, X. H., & Li, S. (2022). Derived Depths in Opaque Waters Using ICESat-2 Photon-Counting Lidar. *Geophy. Res. Lett.*, 49 (22), e2022GL100509. doi: 10.1029/2022GL100509.

[28] Xu, N., Ma, Y., Zhou, H., Zhang, W., Zhang, Z., & Wang, X. H. (2020). A method to derive bathymetry for dynamic water bodies using ICESat-2 and GSWD data sets. IEEE Geosci. *Remote Sens. Lett.*, 19, 1-5. doi: 10.1109/LGRS.2020.3019396.

[29] Hsu, H. J., Huang, C. Y., Jasinski, M., Li, Y., Gao, H., Yamanokuchi, T., Wang, C. G., Chang, T. M., Ren, H., Kuo, C. Y., & Tseng, K. H. (2021). A semi-empirical scheme for bathymetric mapping in shallow water by ICESat-2 and Sentinel-2: A case study in the South China Sea. *ISPRS J. Photogramm. Remote Sens.*, 178, 1-9. doi: 10.1016/j.isprsjprs.2021.05.012.

[30] Guo, X., Jin, X., & Jin, S. (2022). Shallow Water Bathymetry Mapping from ICESat-2 and Sentinel-2 Based on BP Neural Network Model. *Water*, 14 (23), 3862. doi: 10.3390/w14233862.

[31] Austin, R. W., & Petzold, T. J. (1981). The determination of the diffuse attenuation coefficient of sea water using the Coastal Zone Color Scanner. In: Gower, J. F. R. (ed). Oceanography from space. Marine Science, Vol 13. Boston: Springer. pp. 239-56. doi: 10.1007/978-1-4613-3315-9_29.

[32] Jamet, C., Loisel, H., & Dessailly, D. (2012) Retrieval of the spectral diffuse attenuation coefficient K_d (λ) in open and coastal ocean waters using a neural network inversion. *J. Geophys. Res.: Oceans*, 117 (C10). doi: 10.1029/2012JC008076.

[33] Lee, Z. P., Darecki, M., Carder, K. L., Davis, C. O., Stramski, D., & Rhea, W. J. (2005). Diffuse attenuation coefficient of downwelling irradiance: An evaluation of remote sensing methods. *J. Geophys. Res.: Oceans*, 110 (C2). doi: 10.1029/2004JC002573.

[34] Mueller, J. L. (2000). *SeaWiFS algorithm for the diffuse attenuation coefficient, K (490), using water-leaving radiances at 490 and 555 nm*. In: Hooker, S. B., (Ed.). *SeaWiFS postlaunch calibration and validation analyses*, Part 3. Greenbelt; NASA Goddard Space Flight Centre. pp. 24-7.

[35] Morel, A., Huot, Y., Gentili, B., Werdell, P. J., Hooker, S. B., & Franz, B. A. (2007). Examining the consistency of products derived from various ocean color sensors in open ocean (Case 1) waters in the perspective of a multi-sensor approach. *Remote Sens. Environ.*, 111 (1), 69-88. doi: 10.1016/j.rse.2007.03.012.

[36] Sentinel-3 Mission. (2023). Sentinel Online. https://sentinels.copernicus.eu/web/sentinel/user-guides/sentinel-3-olci.

[37] Sentinel-3 User Handbook. (2017). https://filetransfer.itc.nl/pub/dragon4/Optical-Thermal/D2OTP1-Hyperspectral-DOdermatt/references/Sentinel-3_User_Handbook-iss1_v1_20170113.pdf.

[38] Mangin, A., Bourg, L., & d'Andon, O. F. (2010). OLCI level 2 algorithm theoretical basis document: Transparency products. https://sentinel.esa.int/documents/247904/0/OLCI_L2_Transparency_Products.pdf/db679ab6-2547-4a3d-a08d-0ee036a4fb11.

[39] Kyryliuk, D., & Kratzer, S. (2019). Evaluation of Sentinel-3A OLCI products derived using the Case-2 Regional CoastColour processor over the Baltic Sea. *Sensors*, 19 (16), 3609. doi: 10.3390/s19163609.

[40] Glukhovets, D., Kopelevich, O., Yushmanova, A., Vazyulya, S., Sheberstov, S., Karalli, P., & Sahling, I. (2020). Evaluation of the CDOM Absorption Coefficient in the Arctic Seas Based on Sentinel-3 OLCI Data. *Remote Sens.*, 12 (19), 3210. doi: 10.3390/rs12193210.

[41] Valdiya, K. S. (2015). *The making of India: geodynamic evolution*. (2nd edition). Springer. p. 924. doi: 10.1007/978-3-319-25029-8.

[42] Murty, T. S., Flather, R. A., & Henry, R. F. (1986). The storm surge problem in the Bay of Bengal. *Prog. Oceanogr.*, 16 (4), 195-233.

[43] Bhaskaran, P. K., Gayathri, R., Murty, P. L., Bonthu, S., & Sen, D. (2014). A numerical study of coastal inundation and its validation for Thane cyclone in the Bay of Bengal. *Coast Eng.*, 83, 108-18. doi: 10.1016/j.coastaleng.2013.10.005.

[44] Mascarenhas, A. (2004). Oceanographic validity of buffer zones for the east coast of India: A hydrometeorological perspective. *Curr. Sci.*, 86 (3), 399-406. https://www.jstor.org/stable/24108734.

[45] Sarma, V. V., Krishna, M. S., & Srinivas, T. N. (2020). Sources of organic matter and tracing of nutrient pollution in the coastal Bay of Bengal. *Mar. Pollut. Bull.*, 159: 111477. doi: 10.1016/j.marpolbul.2020.111477.

[46] GEBCO Compilation Group (2022). GEBCO_2022 Grid. doi: 10.5285/e0f0bb80-ab44-2739-e053-6c86abc0289c.

[47] Copernicus Data Space Ecosystem. (2023). https://dataspace.copernicus.eu/.

[48] STEP, Science Toolbox Exploitation Platform. (2022). https://step.esa.int/main/.

[49] Hanagan, C., & Mershon, B. (2020). Geoid Height Calculator. UNAVCO: Boulder, CO, USA. https://www.unavco.org/software/geodetic-utilities/geoid-height-calculator/geoid-height-calculator.html.

[50] Ranndal, H., Sigaard Christiansen, P., Kliving, P., Baltazar Andersen, O., & Nielsen, K. (2021). Evaluation of a statistical approach for extracting shallow water bathymetry signals from ICESat-2 ATL03 photon data. *Remote Sens.*, 13 (17), 3548. doi: 10.3390/rs13173548.

[51] Gattuso, J. P., Frankignoulle, M., & Wollast, R. (1998). Carbon and carbonate metabolism in coastal aquatic ecosystems. *Annu. Rev. Ecol. Syst.*, 29 (1), 405-434.

[52] Wetzel, R. G. (2001). *Limnology: Lake and River Ecosystems.* (3rd edition). Academic Press, San Diego, p. 1006.

[53] Gallegos, C., & Moore, K. A. (2000). *Factors contributing to water-column light attenuation*, In: Batiukand, R. A., et al. [Eds.], *Chesapeake Bay submerged aquatic vegetation water quality and habitat-based requirements and restoration targets: A second technical synthesis.* U.S. Environmental Protection Agency, Chesapeake Bay Program, Annapolis, Maryland. pp. 35-54.

[54] Kheireddine, M., Ouhssain, M., Organelli, E., Bricaud, A., & Jones, B. H. (2018). Light absorption by suspended particles in the Red Sea: effect of phytoplankton community size structure and pigment composition. *J. Geophy. Res.: Oceans*, 123 (2), 902-921. doi: 10.1002/2017JC013279.

[55] Davies-Colley, R. J., & Nagels, J. W. (2008). Predicting light penetration into river waters. *J. Geophy. Res.: Biogeosci.*, 113 (G3).

[56] Ackleson, S. G. (1997). *Diffuse attenuation in optically-shallow water: effects of bottom reflectance*. In: Ocean Optics-XIII (Vol. 2963), pp. 326-330. SPIE.

[57] Mishra, D. R., Narumalani, S., Rundquist, D., & Lawson, M. (2005). Characterizing the vertical diffuse attenuation coefficient for downwelling irradiance in coastal waters: Implications for water penetration by high resolution satellite data. *ISPRS J. Photogramm. Remote Sens.*, 60 (1), 48-64. doi: 10.1016/j.isprsjprs.2005.09.003.

[58] Cao, B., Fang, Y., Gao, L., Hu, H., Jiang, Z., Sun, B., & Lou, L. (2021). An active-passive fusion strategy and accuracy evaluation for shallow water bathymetry based on ICESat-2 ATLAS laser point cloud and satellite remote sensing imagery. *Int. J. Remote Sens.*, 42 (8), 2783-2806. doi: 10.1080/01431161.2020.1862441.

[59] Thomas, N., Pertiwi, A. P., Traganos, D., Lagomasino, D., Poursanidis, D., Moreno, S., & Fatoyinbo, L. (2021). Space-borne cloud-native satellite-derived Bathymetry (SDB) models using ICESat-2 and sentinel-2. *Geophy. Res. Lett.*, 48 (6), e2020GL092170. doi: 10.1029/2020GL092170.

[60] Xie, C., Chen, P., Pan, D., Zhong, C., & Zhang, Z. (2021). Improved filtering of ICESat-2 lidar data for nearshore bathymetry estimation using sentinel-2 imagery. *Remote Sens.*, 13 (21), 4303. doi: 10.3390/rs13214303.

[61] Li, S., Wang, X. H., Ma, Y., & Yang, F. (2023). Satellite-Derived Bathymetry with Sediment Classification Using ICESat-2 and Multispectral Imagery: Case Studies in the South China Sea and Australia. *Remote Sens.*, 15 (4), 1026. doi: 10.3390/rs15041026.

[62] Eidam, E., Walker, C., Bisson, K., Paris, M., & Cooper, L., (2022). *Novel application of ICESat-2 ATLAS data to determine coastal light attenuation as a proxy for suspended particulate matter*. In: OCEANS 2022. Hampton Roads, VA, USA. pp. 1-7, doi: 10.1109/OCEANS47191.2022.9977084.

[63] Zhang, X., Ma, Y., Li, Z., & Zhang, J. (2022). Satellite derived bathymetry based on ICESat-2 diffuse attenuation signal without prior information. *Int. J. App. Earth Obs. Geoinform.*, 113, 102993. doi: 10.1016/j.jag.2022.102993.

[64] Xie, H., Sun, Y., Liu, X., Xu, Q., Guo, Y., Liu, S.,... & Tong, X. (2021). Shore Zone Classification from ICESat-2 Data over Saint Lawrence Island. *Mar. Geod.*, 44 (5), 454-466. doi: 10.1080/01490419.2021.1898498.